

Article

# Development of a Refractory High Entropy Superalloy

Oleg N. Senkov <sup>1,\*</sup>, Dieter Isheim <sup>2</sup>, David N. Seidman <sup>2</sup> and Adam L. Pilchak <sup>1</sup>

<sup>1</sup> Air Force Research Laboratory, Materials and Manufacturing Directorate, Wright-Patterson AFB, OH 45433, USA; adam.pilchak.1@us.af.mil

<sup>2</sup> Department of Materials Science and Engineering and Northwestern University Center for Atom-Probe Tomography, Northwestern University, 2220 Campus Drive, Evanston, IL 60208, USA; isheim@northwestern.edu (D.I.); d-seidman@northwestern.edu (D.N.S.)

\* Correspondence: oleg.senkov.ctr@us.af.mil; Tel.: +1-937-255-4064

Academic Editor: An-Chou Yeh

Received: 12 February 2016; Accepted: 2 March 2016; Published: 17 March 2016

**Abstract:** Microstructure, phase composition and mechanical properties of a refractory high entropy superalloy, AlMo<sub>0.5</sub>NbTa<sub>0.5</sub>TiZr, are reported in this work. The alloy consists of a nano-scale mixture of two phases produced by the decomposition from a high temperature body-centered cubic (BCC) phase. The first phase is present in the form of cuboidal-shaped nano-precipitates aligned in rows along <100>-type directions, has a disordered BCC crystal structure with the lattice parameter  $a_1 = 326.9 \pm 0.5$  pm and is rich in Mo, Nb and Ta. The second phase is present in the form of channels between the cuboidal nano-precipitates, has an ordered B2 crystal structure with the lattice parameter  $a_2 = 330.4 \pm 0.5$  pm and is rich in Al, Ti and Zr. Both phases are coherent and have the same crystallographic orientation within the former grains. The formation of this modulated nano-phase structure is discussed in the framework of nucleation-and-growth and spinodal decomposition mechanisms. The yield strength of this refractory high entropy superalloy is superior to the yield strength of Ni-based superalloys in the temperature range of 20 °C to 1200 °C.

**Keywords:** refractory high entropy alloy; superalloy; microstructure and phase analysis; mechanical properties

## 1. Introduction

Future hypersonic vehicles and turbine engines will require revolutionary new structural alloys, which can survive extreme temperature and loading conditions, are simultaneously ductile and tough, and are able to meet unusually demanding design requirements [1]. Current high-temperature ceramics and intermetallics are incapable of meeting these requirements due to low toughness, while advanced Ni-based superalloys are approaching possible extreme property combinations with respect to their evolution and development; *i.e.*, they still suffer from high density and their maximum temperature use is limited by melting at ~1250–1300 °C. New metallic materials with higher melting points, such as W-based alloys hardened with HfC precipitates [2], Co-Re- or Co-Al-W-based alloys [3] or two-phase (FCC + L<sub>12</sub>) refractory superalloys based on platinum group metals (Os, Ru, Ir, Rh or Pt) [4,5], have been examined for use beyond Ni-based superalloys. The extremely high density and/or the cost of these new alloys are, however, the main obstacles.

The concept of high entropy alloys (HEAs) is one of the most recent developments in material science [6]. Depending on their compositions and microstructures, HEAs offer a diverse range of attractive properties, such as high microhardness and wear resistance, exceptional mechanical properties and oxidation resistance [7–9]. HEA has initially been defined as an alloy consisting of five or more principle elements, each with concentration between 5 and 35 atom percent [6]. Later, an additional

requirement has been added according to which HEA is an alloy whose ideal configurational entropy of mixing,  $\Delta S_{\text{conf}} = -R \sum X_i \ln(X_i)$ , is equal to or higher than  $1.5R$  [9,10]. Here,  $X_i$  is the atom fraction of element  $i$  and  $R$  is the gas constant. A high entropy of mixing of the alloying elements is thought to reduce the driving force for the formation of intermetallic phases and hence favors the formation of solid-solution phases. There is, however, experimental evidence that ordered solid-solutions and/or intermetallic phases may also exist in many HEAs, which strongly affect their microstructures and properties [9,11–13].

Using the HEA concept, several refractory high entropy alloys (RHEAs) with attractive combinations of room temperature and elevated temperature mechanical properties and oxidation resistance, have recently been reported as promising alternatives to Ni-based superalloys [11,14–20]. In spite of the compositional complexity, the number of phases observed in these alloys does not generally exceed two or three, with the BCC solid-solution typically being the primary phase. RHEAs with a low density and high strength are among the most promising recent achievements in this field [19–23]. In particular, the density of these new alloys is in the range of 5.9 to 8.4 g/cm<sup>3</sup> and their specific strengths are often superior to Ni-based superalloys [19,23]. Recent studies indicate that some of these alloys consist of very fine, nano-scale mixtures of two BCC phases with similar lattice parameters, which may be responsible for their high strengths [19].

In this research, the results of detailed analyses of the microstructure and properties of a recently reported two-phase AlMo<sub>0.5</sub>NbTa<sub>0.5</sub>TiZr RHEA [19,20] are presented. It was found that the alloy consists of a nano-scale, modulated mixture of ordered B2 and disordered BCC coherent phases, which has high temperature stability and high strength. This microstructure looks similar to a rafted microstructure of Ni-based superalloys consisting of cuboids with the ordered L1<sub>2</sub> structure embedded in an FCC solid-solution matrix. Based on this microstructural similarity, as well as its complex composition and very high strength sustained at high temperatures, we call this two-phase alloy a “refractory high entropy superalloy”.

## 2. Materials and Methods

The AlMo<sub>0.5</sub>NbTa<sub>0.5</sub>TiZr alloy was prepared by vacuum arc melting nominal mixtures of the constituent elements. The purities of aluminum, molybdenum, niobium, tantalum, titanium and zirconium were 99.999%, 99.99%, 99.95%, 99.9%, 99.98% and 99.95%, respectively. The details of the alloy preparation are given elsewhere [19]. The actual alloy composition, determined with inductively-coupled plasma-optical emission spectroscopy (ICP-OES), is given in Table 1. After solidification, the AlMo<sub>0.5</sub>NbTa<sub>0.5</sub>TiZr alloy was hot isostatic pressed (HIPed) at 1400 °C and 207 MPa for 2 h, and then annealed at 1400 °C for 24 h in continuously flowing high-purity argon. During HIPing and annealing, the alloy was covered with a Ta foil to minimize oxidation. The cooling rate after annealing was 10 °C/min. The crystal structure was identified utilizing an X-ray diffractometer, with Cu K<sub>α</sub> radiation, and a 2 $\theta$  scattering range of 10° to 140°. A Quanta 600F SEM (FEI, North America NanoPort, Hillsboro, OR, USA) was used to study the microstructure employing backscatter electron (BSE) and electron backscatter diffraction (EBSD) modes.

**Table 1.** Chemical composition (at.%) of the AlMo<sub>0.5</sub>NbTa<sub>0.5</sub>TiZr superalloy.

Element	Al	Mo	Nb	Ta	Ti	Zr
Composition	20.4	10.5	22.4	10.1	17.8	18.8

Atom-probe tomography (APT) [24–26] was used to analyze the fine microstructure and determine the phase compositions locally with sub-nanometer scale spatial resolution. For preparing sharp nanotips suitable for APT, a standard lift-out, mounting and nanotip sharpening technique was utilized [27,28] employing a FEI Helios 600 Nanolab focused-ion beam (FIB) microscope. Figure 1 exhibits different stages during the preparation of APT nanotips from the AlMo<sub>0.5</sub>NbTa<sub>0.5</sub>TiZr alloy,

with the basket-weave pattern of precipitates continuously visible. The APT was performed employing a LEAP4000X S tomograph, CAMECA Instruments, Madison, WI. To field-evaporate elements from a nanotip, essentially one atom at a time, a picosecond ultraviolet pulse laser (wavelength = 355 nm), with an energy per pulse of 30 pJ, a pulse repetition rate of 250 kHz, and a target detection rate of 0.02 to 0.03 ion/pulse, were employed. LEAP tomographic analyses were performed at a specimen temperature of 32 K at a background vacuum of  $< 2 \times 10^{-11}$  Torr. The obtained results were analyzed utilizing the IVAS version 3.6.12 software package (CAMECA Instruments, Inc., Madison, WI, USA).

Compression tests of rectangular specimens with the dimensions of  $\sim 4.7 \text{ mm} \times 4.7 \text{ mm} \times 7.7 \text{ mm}$  were performed using a computer-controlled Instron (Instron, Norwood, MA, USA) mechanical testing machine outfitted with a Brew vacuum furnace and silicon carbide dies. A constant ramp speed that corresponded to an initial strain rate of  $10^{-3} \text{ s}^{-1}$  was utilized. The deformation of all specimens was video recorded and the image correlation software Vic-Gauge (Correlated Solutions, Inc., Columbia, SC, USA) was employed to register strain *versus* stress curves.

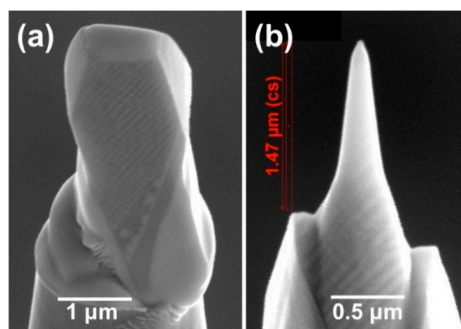


**Figure 1.** SEM micrographs of Atom-probe tomography (APT) nanotip preparation from the  $\text{AlMo}_{0.5}\text{NbTa}_{0.5}\text{TiZr}$  alloy by focused-ion beam (FIB) microscopy-based lift-out, mounting and sharpening process. (a) lift-out volume mounted on a silicon micropost; (b) Final APT nanotip after FIB  $\text{Ga}^+$  ion milling with annular patterns. The basket-weave pattern of the precipitates is visible during the entire FIB preparation process.

### 3. Results

#### 3.1. Microstructure Analysis

According to the X-ray diffraction analysis, Figure 2a, the annealed alloy consists of two BCC phases. One phase has the lattice parameter  $a_1 = 326.9 \pm 0.5 \text{ pm}$  and another phase has the lattice parameter  $a_2 = 330.4 \pm 0.5 \text{ pm}$ , which indicates an  $\sim 1.07\%$  lattice parameter mismatch. After 50% compression deformation at  $1000 \text{ }^\circ\text{C}$ , the lattice parameters of the phases change slightly:  $a_1 = 326.1 \pm 0.5 \text{ pm}$  and  $a_2 = 331.2 \pm 0.5 \text{ pm}$  (Figure 2b).

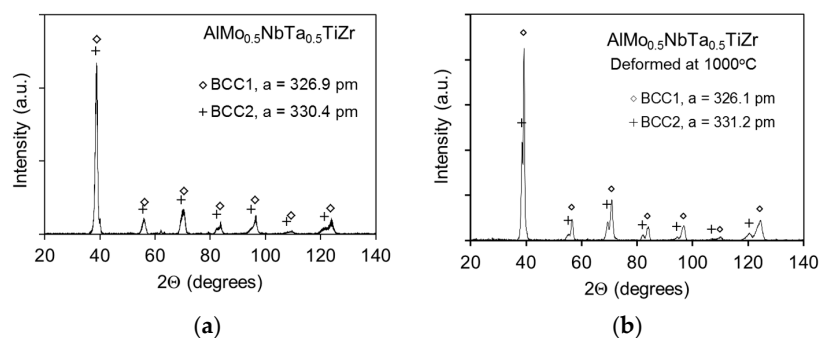


**Figure 2.** X-ray diffraction patterns of  $\text{AlMo}_{0.5}\text{NbTa}_{0.5}\text{TiZr}$ : (a) after annealing at  $1400 \text{ }^\circ\text{C}$  and (b) after following 50% compression deformation at  $1000 \text{ }^\circ\text{C}$ .

After HIPing and annealing, the  $\text{AlMo}_{0.5}\text{NbTa}_{0.5}\text{TiZr}$  alloy has an equiaxed grain structure, with an average grain size of  $75\ \mu\text{m}$  (Figure 3). Subgrain boundaries with misorientation angles of less than  $1.5^\circ$  are present inside grains. Large second-phase precipitates, which appear dark in a BSE image, are observed at the grain boundaries. Their volume fraction is  $\sim 6\%$  and they are rich in Al and Zr. High magnification SEM/BSE images reveal the presence of a fine, basket-weave, nano-lamellar structure inside the grains (Figure 4a). This basket-weave nano-structure consists of two-phases and the lamellar spacing is estimated to be  $\sim 70\ \text{nm}$ . The nano-precipitates coarsen at grain- and sub-grain boundaries and reveal two phases with distinct Z-contrast (Figure 4b). The EDS analyses of the coarsened precipitates demonstrate that the bright phase is rich in Mo, Nb and Ta, while the dark phase is rich in Al and Zr. Because of the very small dimensions of the precipitates, quantitative chemical analysis of individual precipitates using SEM was not possible. An SEM/EBSD analysis confirmed that the two phases have BCC crystal structures and the same crystallographic orientations inside every grain.

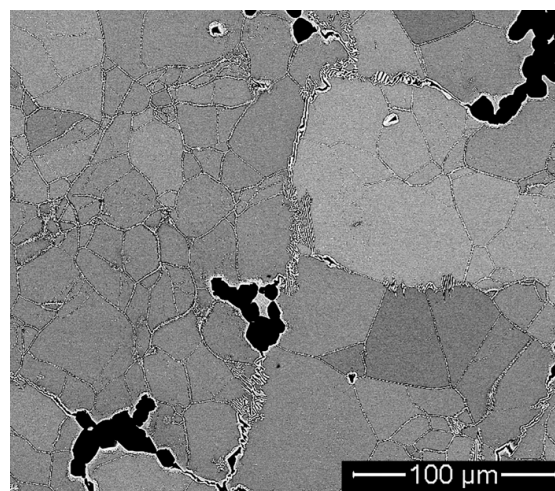


**Figure 3.** SEM/backscatter electron (BSE) image of equiaxed grain structure of  $\text{AlMo}_{0.5}\text{NbTa}_{0.5}\text{TiZr}$  after annealing at  $1400\ ^\circ\text{C}$  for 24 h. Second-phase precipitates (which are dark) are present at grain boundaries.

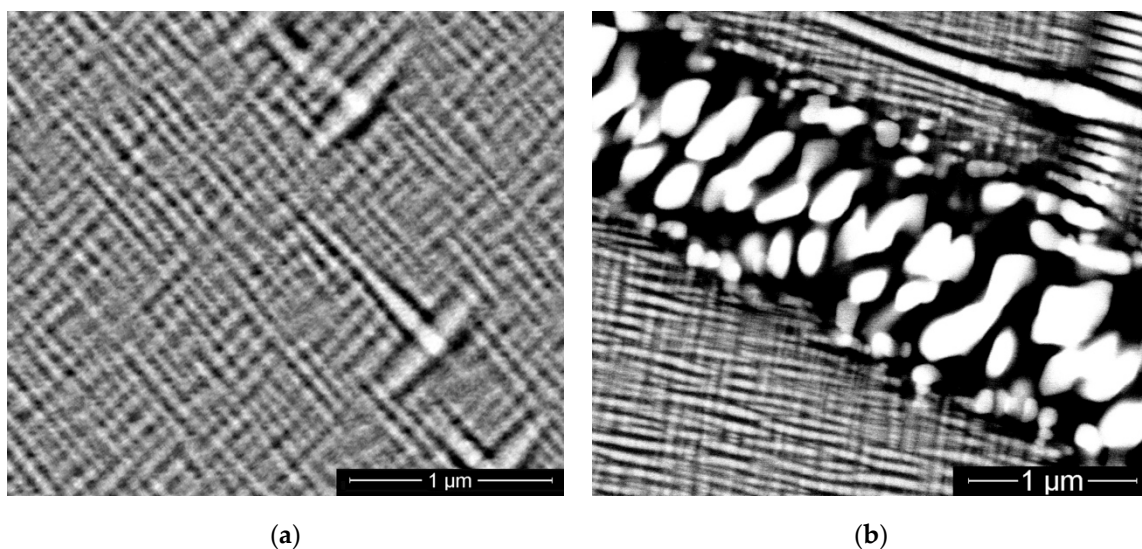


**Figure 4.** High magnification SEM/BSE images of: (a) a two-phase basket-weave lamellar structure inside grains and (b) coarsened particles of the two phases at grain boundaries in  $\text{AlMo}_{0.5}\text{NbTa}_{0.5}\text{TiZr}$ .

To reveal the morphology of the fine nano-structure inside grains, as well as the level of ordering of the two phases, scanning transmission electron microscopy (STEM) and regular TEM imaging and electron diffraction were performed at Ohio State University, group of Professor H. Fraser [29]. The STEM analysis demonstrates that the microstructure consists of two phases (Figure 5). One phase is present in the form of cuboidal-shaped or plate-like precipitates and has a disordered BCC crystal structure. Another phase has an ordered B2 structure and is present in the form of continuous thin channels between these precipitates and thicker knots observed at the intersections of the channels. A dark-field TEM image taken in the diffraction condition of an indexed super-lattice reflection of the B2 phase indicates that this reflection belongs to illuminated channels, whereas the cuboidal-shaped phase don't exhibit contrast and is likely disordered, Figure 6.

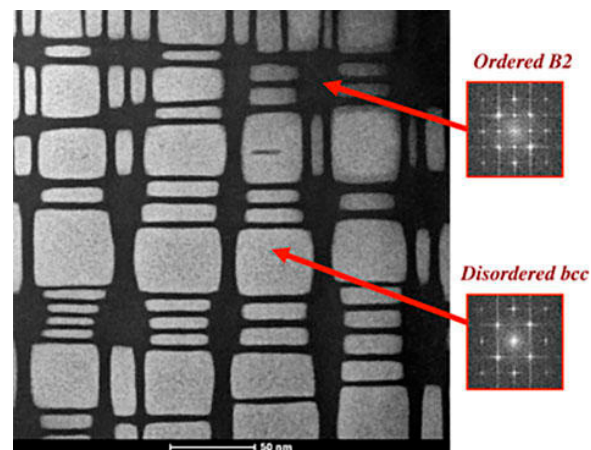


**Figure 5.** Scanning transmission electron microscopy (STEM) high-angle annular dark-field image and fast Fourier transforms (inside the red squares) recorded from a survey sample extracted from the inside-grain region ([29], reprinted by permission of Taylor & Francis Ltd.).

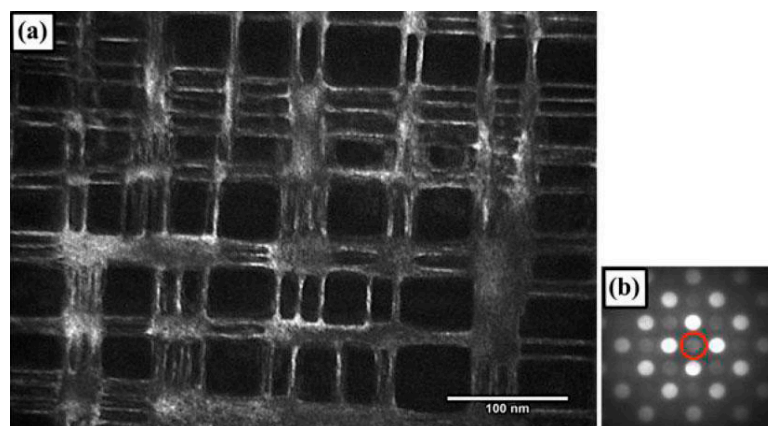


**Figure 6.** (a) Dark-field TEM micrograph of the nano-phase structure of  $\text{AlMo}_{0.5}\text{NbTa}_{0.5}\text{TiZr}$ ; and (b) respective selected area diffraction pattern. The dark field image was obtained with a (001) superlattice reflection placed inside the objective aperture (indicated by the circle) ([29], reprinted by permission of Taylor & Francis Ltd.).

We note that all the cuboidal-shaped and plate-like precipitates have the same crystallographic orientation inside one grain and their edges are parallel to  $\langle 100 \rangle$  directions. The precipitate dimensions in two orthogonal directions parallel to the precipitate edges vary from  $\sim 10$  to  $\sim 55$  nm and from  $\sim 25$  to  $\sim 55$  nm, respectively. The width of the matrix channels is  $\sim 7.0 \pm 1.0$  nm. The volume fraction of the disordered BCC phase is estimated to be  $62 \pm 5\%$ .

### 3.2. Atom-Probe Tomographic Analyses

Figure 7 displays an APT reconstruction of the precipitate microstructure in the  $\text{AlMo}_{0.5}\text{NbTa}_{0.5}\text{TiZr}$  alloy. An 18 at.% Ta isoconcentration surface is superposed (red) to outline and highlight the two-phase structure with precipitates rich in Ta, Nb and Mo, and channels rich in Al, Ti and Zr. To provide a 3D impression of the precipitate microstructure, the reconstruction box is displayed in Figure 7a as seen from the front, and in Figure 7b projected from the top. The precipitates have a cuboidal shape and form long rows with the thin matrix channels between the precipitates. A detailed 3D analysis indicates that while some precipitates have a near equiaxed morphology approximating a cube, others resemble thin rectangular plates. Occasionally, gaps (they are called knots in Section 3.1) consisting of the matrix phase interrupt a row of cuboidal precipitates (Figure 7a). Larger, long matrix-channels separate entire groups of precipitate rows (Figure 7b). These large and long matrix channels are most likely responsible for the contrast observed in the backscatter SEM micrographs (Figure 4), which suggests a basket-weave structure with a barely resolved substructure that matches in scale with the individual cuboidal precipitates observed in the 3D APT reconstruction.

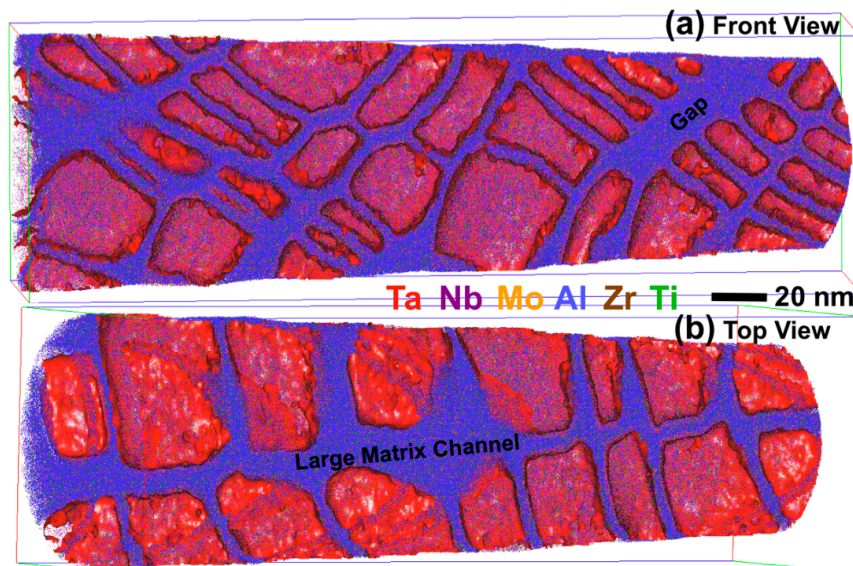


**Figure 7.** APT reconstruction of the precipitate microstructure in the  $\text{AlMo}_{0.5}\text{NbTa}_{0.5}\text{TiZr}$  alloy in a rectangular parallel piped volume,  $93 \times 93 \times 301 \text{ nm}^3$  in size, containing 41,677,323 atoms, (a) front view and (b) top view of the reconstructed volume. An 18 at.% Ta isoconcentration surface is superposed in red to outline the Ta-rich cuboidal precipitates. For clarity, only 40% of the Al atoms are shown, and only 5% of the atoms of all other elements.

The concentration profiles were obtained for all constituent elements inside a cylinder crossing a row of cuboidal precipitates separated by matrix channels, as indicated in the volume on top of Figure 8, with the volume shown in the same projection as in Figure 7a. The concentration profiles of the alloying elements along the cylinder are displayed in Figure 8, and the average composition of the alloying elements is listed in Table 2. The precipitates are rich in Mo, Nb and Ta (15.6, 31.8 and 21.9 at.%, respectively), and depleted in Al, Ti and Zr (3.7, 17.2 and 9.5 at.%, respectively), whereas the thin matrix channels are rich in Al, Ti and Zr (12.1, 19.2 and 15.8 at.%, respectively) and depleted in Mo, Nb and Ta (11.7, 25.8 and 15.2 at.%, respectively). By comparing the concentrations of Mo, Nb and Ta in the cuboids and thin matrix channels with the average concentrations of these elements in the box studied (about 10.1, 21.0 and 10.6 at.%, respectively), it is clear that the precipitates and thin channels contain higher concentrations of these elements relative to the average concentrations. This should indicate the elemental partitioning on a scale larger than an individual precipitate. Indeed,

a compositional analysis of the gap region (Figure 7a) and the large long matrix channel (Figure 7b) reveals that these regions are depleted in Mo, Nb and Ta (and rich in Al, Ti and Zr) far more than the thin matrix channels in the rows of cuboidal precipitates displayed in Figure 7, with the quantitative concentrations presented in Table 2. The different compositions of the wide (large) and thin (small) channels of the matrix phase can be explained by a rather broad compositional interface between these two phases, with a transition layer width of ~2–4 nm inside the channels.

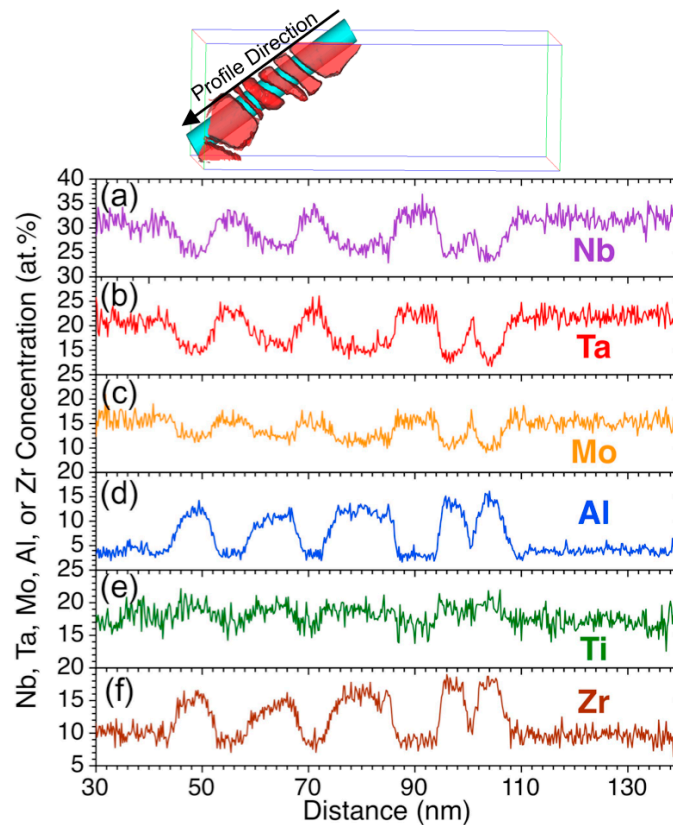


**Figure 8.** Concentration profiles of Nb, Ta, Mo, Al, Ti and Zr through a row of aligned cuboidal precipitates. The concentration profiles were taken along the cylinder positioned in the reconstruction box cutting through the precipitates displayed. The reconstruction volume is seen in the same projection direction as in Figure 7a, with only the precipitates used for these concentration profiles displayed. The average compositions of cuboidal precipitates and the thin matrix channels between them are listed in Table 2.

**Table 2.** Results of the APT compositional analysis. The overall (average) chemical composition of the  $\text{AlMo}_{0.5}\text{NbTa}_{0.5}\text{TiZr}$  alloy in the analyzed volume containing 41,677,323 atoms, and local chemical compositions of the precipitates and matrix channels in at.%.

Region	Al	Mo	Nb	Ta	Ti	Zr
Overall APT reconstruction <sup>1</sup>	17.6	10.1	21.0	10.6	20.9	19.6
Cuboidal precipitates <sup>2</sup>	3.7	15.6	31.8	21.9	17.2	9.5
Thin matrix channels between precipitates <sup>2</sup>	12.1	11.7	25.8	15.2	19.2	15.8
Large long matrix channel <sup>2</sup>	25.9	5.5	14.2	4.0	24.1	25.9
Large gap in cuboidal row <sup>2</sup>	26.1	7.7	13.7	3.7	24.1	24.1

<sup>1</sup> Statistical error < 0.01 at.%; <sup>2</sup> Statistical error < 0.1 at.%.

### 3.3. Mechanical Properties

In the annealed condition,  $\text{AlMo}_{0.5}\text{NbTa}_{0.5}\text{TiZr}$  has very high Vickers microhardness ( $H_v = 5.8 \pm 0.1$  GPa), compression yield strength ( $\sigma_{0.2} = 2000$  MPa) and fracture strength ( $\sigma_p = 2368$  MPa), while exhibiting limited compression ductility ( $\delta = 10\%$ ) at 23 °C. With an increase in temperature, the strength decreases, while the compression ductility increases (Table 3). Upon heating from 23 °C to 800 °C, the alloy loses about 20% of its room temperature strength. In the temperature range between 800 °C and 1000 °C, a ~57% decrease in strength occurs; the yield strength is still, however, very high at 1000 °C ( $\sigma_{0.2} = 745$  MPa). A further increase in temperature to 1200 °C results in the yield strength decreasing to  $\sigma_{0.2} = 250$  MPa.

**Table 3.** Compression yield strength,  $\sigma_{0.2}$ , maximum strength,  $\sigma_p$ , and fracture strain,  $\delta$ , of the  $\text{AlMo}_{0.5}\text{NbTa}_{0.5}\text{TiZr}$  RHEA superalloy at different temperatures.

T, °C	$\sigma_{0.2}$ , MPa	$\sigma_p$ , MPa	$\delta$ , %
23	2000	2368	10
600	1870	2210	10
800	1597	1810	11
1000	745	772	> 50
1200	250	275	> 50

X-ray diffraction analysis demonstrates that the deformed samples retain the two-phase BCC crystal structure, with almost the same lattice parameters, as prior to the deformation (Figure 2). After 50% compression deformation at 1000 °C and 1200 °C, the matrix grains become elongated in the directions of plastic flow, which are inclined by ~90° to 60° to the compression direction. The basket-weave nano-phase structure coarsens (compare Figure 9a with Figure 4a) and a characteristic relief forms inside the deformed grains (Figure 9b). This relief is likely a result of interaction of the local material flow with the interface boundaries between the nano-phases.

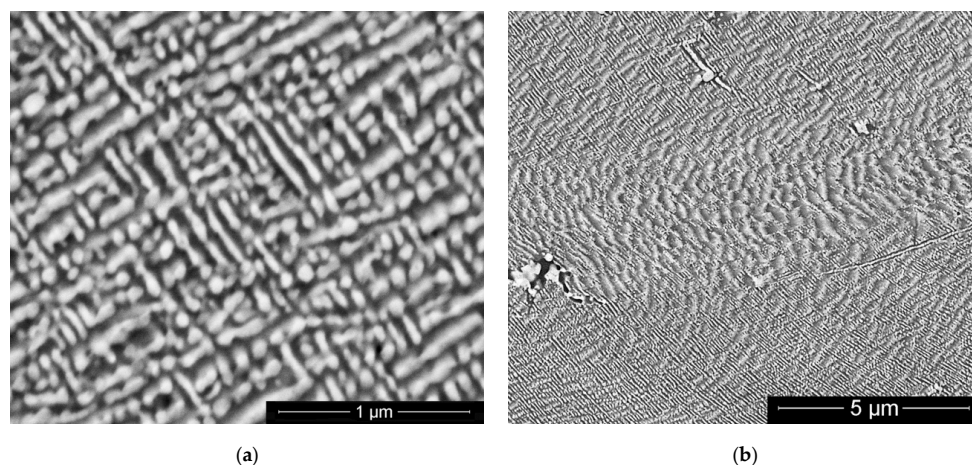


**Figure 9.** SEM/BSE images of the basket-weave nano-phase structure (at two different magnifications) in  $\text{AlMo}_{0.5}\text{NbTa}_{0.5}\text{TiZr}$  after 50% compression deformation at 1000 °C.

## 4. Discussion

Microstructural analyses indicate that the  $\text{AlMo}_{0.5}\text{NbTa}_{0.5}\text{TiZr}$  RHEA was essentially a single-phase BCC structure at the annealing temperature, 1400 °C. This is confirmed by the SEM and EBSD results, which reveal a high-temperature coarse-grained structure (Figure 3). During slow cooling, after annealing, this high-temperature BCC phase experiences a phase transformation with formation of a very fine, nano-scaled mixture of two coherent phases with the BCC and B2 structures

inside the former grains. One of these phases (BCC) is rich in Mo, Nb and Ta, and another phase (B2) is rich in Al, Ti and Zr. This phase transformation is similar to that observed in Ta-Zr or Nb-Zr binary alloys, within the composition range of the miscibility gap between two BCC solid solutions at temperatures above the eutectoid transformation in these systems [30]. Though the resulting phases are disordered BCC solid solutions in the binary systems, in the  $\text{AlMo}_{0.5}\text{NbTa}_{0.5}\text{TiZr}$  superalloy only one phase, rich in refractory elements, has a disordered BCC crystal structure, while another phase, rich in Al, Ti and Zr, has an ordered B2 crystal structure. The ordering is likely due to strong interactions of Al atoms with Ti and Zr atoms, so that Ti and Zr tend to occupy one sub-lattice, while Al and the other elements prefer the other sub-lattice. The chemical composition of the B2 phase supports this assumption (Table 2), in that the combined concentrations of Ti and Zr equal about 50 at.%. Using the chemical composition data from Table 2, the average atomic numbers of elements in cuboidal precipitates, thin matrix channels and large matrix channels are estimated to be 43.6, 38.7 and 30.1, respectively, and the average atomic radii of the elements are estimated to be 143.7 pm, 145.3 pm and 147.0 pm, respectively. These differences in the average atomic numbers agree with the observed Z-contrasts of the phases in the SEM/BSE and STEM images (Figures 4 and 5). A comparison of the average atomic radii with the measured lattice parameters allows us to conclude that the disordered BCC phase forming cuboidal precipitates has a slightly smaller lattice parameter than the ordered B2 phase forming the channels.

The decomposition microstructure in  $\text{AlMo}_{0.5}\text{NbTa}_{0.5}\text{TiZr}$  possesses several striking features. There is a strong periodicity of the nano-phase microstructure in the  $\langle 100 \rangle$ -directions. Along these directions, the precipitates are structured first on a larger length scale, approximately 70 nm, as seen in the basket-weave structure by SEM/BSE (Figure 4). Additionally, the basket-weave structure has a second-level of structure, the thin matrix channels on a 5–10 nm scale dividing the basket-weave into individual cuboidal precipitates, resolved by TEM (Figures 5 and 6) and APT (Figures 7 and 8). Both phases share the same base crystal structure (BCC), have similar lattice parameters, and have the same crystallographic orientations within a single grain of the high-temperature BCC phase from which these phases formed. These microstructural features are very similar to the rafted microstructure observed commonly in Ni-base superalloys, consisting of cuboidal precipitates with the ordered  $\text{L}_{12}$  structure in a disordered FCC solid solution matrix [31]. Based on this microstructural similarity and the very high strength sustained at high temperatures, we call this two-phase  $\text{AlMo}_{0.5}\text{NbTa}_{0.5}\text{TiZr}$  alloy a “refractory high entropy superalloy”. The rafting in Ni-base superalloys is driven by elastic interactions between individual precipitates, and the approximately 1% lattice misfit between the BCC and B2 phases most likely causes similar crystallographic alignments of the cuboidal-shaped precipitates in the  $\text{AlMo}_{0.5}\text{NbTa}_{0.5}\text{TiZr}$  superalloy.

There is, however, a fundamental difference between the nano-phase structures formed in Ni-based superalloys and in the  $\text{AlMo}_{0.5}\text{NbTa}_{0.5}\text{TiZr}$  superalloy. The precipitation in Ni-based superalloys is controlled by the nucleation and growth mechanism, which, during cooling from a supersolvus temperature, results in multi-modal distributions consisting of micron-sized primary, submicron-sized secondary and nanometer-sized tertiary precipitates [31]. In contrast, the formation of secondary or tertiary generations of precipitates is not observed in the  $\text{AlMo}_{0.5}\text{NbTa}_{0.5}\text{TiZr}$ . Furthermore, large matrix channels in  $\text{AlMo}_{0.5}\text{NbTa}_{0.5}\text{TiZr}$  are much more depleted in the refractory elements than the narrow thin channels and are not capable of producing the refractory-rich precipitates. These observations indicate that an additional, spinodal decomposition mode [32–35] may be operative in  $\text{AlMo}_{0.5}\text{NbTa}_{0.5}\text{TiZr}$  during the first stage of decomposition upon continuous cooling from 1400 °C. This spinodal decomposition produces periodic compositional wave patterns defining the larger, ~70 nm scale of the basket-weave structure observed here, with significant compositional separation of Mo, Nb and Ta, which diffuse towards the wave peaks, from Al, Ti and Zr, which diffuse towards the wave valleys. Upon further cooling, the second decomposition stage occurs in the compositional wave regions rich in the refractory elements, with the formation of cuboidal BCC precipitates separated by thin B2 channels, while the wave regions rich in Al, Ti and Zr do not experience further phase

transformations and are retained as thick matrix channels with the B2 crystal structure. Atomic ordering during the spinodal decomposition has already been observed, e.g., in a Fe-Be alloy [36].

The specific morphology of the two-phase structure (*i.e.*, continuous channels of the matrix phase surrounding cuboidal nano-precipitates) was predicted earlier by computer simulations of spinodal decomposition using a dynamic model, which takes into account elastic effects, such as different elastic stiffnesses of the phases, cubic elastic anisotropy, and coherent elastic misfit between the phases [35,37]. In particular, this model predicts that the softer phase always wraps stiffer precipitates and a small lattice misfit results in cuboidal shapes of the precipitates [37]. Although experimental information on the elastic moduli of the BCC and B2 phases in  $\text{AlMo}_{0.5}\text{NbTa}_{0.5}\text{TiZr}$  is unavailable, the rule-of-mixture estimates suggest that the cuboidal precipitates should be stiffer than the channels. For example, the estimated bulk modulus of the BCC phase is 164 GPa, and that of the B2 phase is 115 GPa.

The very high strength of the alloys is likely due to the nano-scaled mixture of two coherent phases with ordered and disordered crystal structures, because a high volume fraction of the heterophase boundaries between the phases impedes the deformation flow. The high thermal stability of this two-phase nanostructure permits this refractory high entropy superalloy to retain its high strength at temperatures up to 1200 °C, with a yield strength and specific yield strength much greater than those of Ni-based superalloys in the temperature range from 20 to 1200 °C (Figure 10).

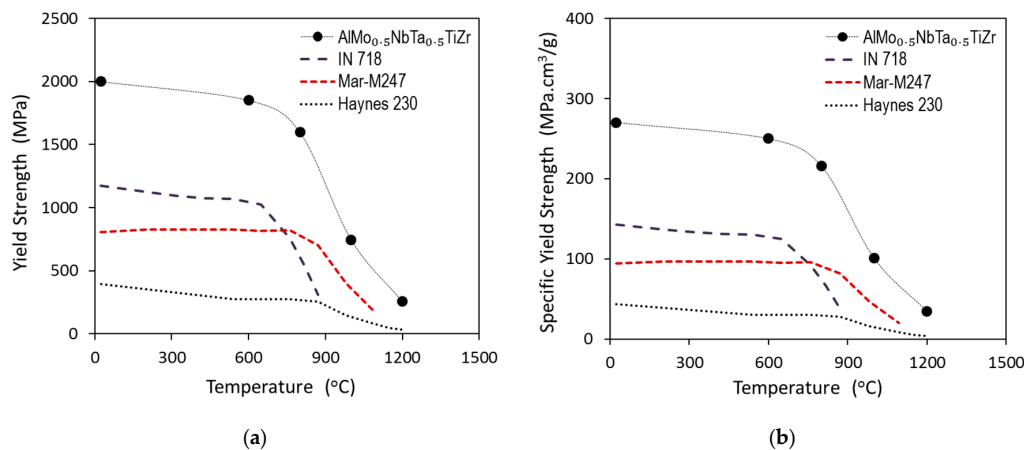


**Figure 10.** Comparison of the temperature dependences of: (a) yield strength and (b) specific yield strength of the RHEA superalloy  $\text{AlMo}_{0.5}\text{NbTa}_{0.5}\text{TiZr}$  and three Ni-based superalloys: precipitation strengthened IN718 [38] and Mar-M247 [39], and solid solution-strengthened Haynes<sup>®</sup> 230 [40].

## 5. Conclusions

The microstructure and mechanical properties of a refractory high entropy superalloy,  $\text{AlMo}_{0.5}\text{NbTa}_{0.5}\text{TiZr}$ , are reported in this work. After annealing at 1400 °C and slow cooling to room temperature, the superalloy microstructure consists of cuboidal nano-precipitates with a disordered BCC crystal structure and two types of thin and large channels or gaps of an ordered B2 phase between these precipitates. The average edge length and volume fraction of the cuboidal precipitates are  $\sim 30$  nm and  $62 \pm 5\%$ , respectively, and the average thickness of the thin channels is  $\sim 7$  nm. The disordered BCC precipitates are rich in Mo, Nb and Ta, and its lattice parameter is  $a_1 = 326.9$  pm. The ordered B2 phase is rich in Al, Ti and Zr, and its lattice parameter is  $a_2 = 330.4$  pm. Both phases are coherent and have the same crystallographic orientation inside former grains of a high-temperature phase. The small lattice mismatch (1.07%) between the phases is likely responsible for the specific morphology and high thermal stability of this nano-phase structure. The superalloy has exceptionally high yield strength, which is superior to the strength of Ni superalloys in the temperature range of 20 °C to 1200 °C. It is suggested that the two-phase, BCC/B2 nano-structure is responsible for the high strength and hardness of the  $\text{AlMo}_{0.5}\text{NbTa}_{0.5}\text{TiZr}$  superalloy.

**Acknowledgments:** Discussions with D. Miracle and C. Woodward are much appreciated. Work by ONS was supported through the Air Force on-site contract No. FA8650-15-D-5230 conducted by UES, Inc., Dayton, Ohio. Inductively-coupled plasma-optical emission spectroscopy, X-ray diffraction, SEM and mechanical testing were conducted at the Air Force Research Laboratory (AFRL). Transmission Electron Microscopy was conducted at the Ohio State University, Columbus, Ohio, and the permission of the authors of Ref. [29] and the publisher (Taylor & Francis Ltd, www.tandfonline.com) to publish Figures 5 and 6 is appreciated. Atom-probe tomography was performed at the Northwestern University Center for Atom-Probe Tomography (NUCAPT). The LEAP tomograph at NUCAPT was purchased and upgraded with funding from NSF-MRI (DMR-0420532) and ONR-DURIP (N00014-0400798, N00014-0610539, N00014-0910781) grants. Instrumentation at NUCAPT was supported by the Initiative for Sustainability and Energy at Northwestern University. This research made use of Northwestern's NUANCE-EPIC facility. NUCAPT and EPIC received support from the MRSEC program (NSF DMR-1121262) through Northwestern's Materials Research Center. EPIC received support from the International Institute for Nanotechnology (IIN); and the State of Illinois, through the IIN.

**Author Contributions:** All the authors contributed equally to the discussion of the results and writing the paper. Oleg N. Senkov developed the alloy, coordinated the research, and conducted microstructure and mechanical property testing and analysis. Dieter Isheim and David N. Seidman performed the APT experiments and APT data analysis. Adam L. Pilchak coordinated work at the AFRL and provided conceptual advises.

**Conflicts of Interest:** The authors declare no conflicts of interest.

## Abbreviations

The following abbreviations are used in this manuscript:

APT	atom-probe tomography
BCC	body-centered cubic
BSE	back-scattered electron
EBSD	electron backscatter diffraction
FCC	face-centered cubic
FIB	focus ion beam
HEA	high entropy alloy
HIP	hot isostatic pressing
RHEA	refractory high entropy alloy
SEM	scanning electron microscopy
STEM	scanning transmission electron microscopy
TEM	transmission electron microscopy

## References

1. Neergaard, L.J.; Pasilio, C.L.; Witeof, Z.; Shelton, A. Materials data requirements for design of an expendable hypersonic airbreathing airframe. In Proceedings of Joint Army Navy NASA Air Force, Albuquerque, NM, USA, 8–12 December 2014.
2. Brown, W.F.; Mindin, H.; Ho, C.Y. *Aerospace Structural Metals Handbook*; CINDAS/Purdue University: West Lafayette, IN, USA, 1992; Volume 5, p. 4218 and p. 5502.
3. Gorr, B.; Christ, H.J.; Mukherji, D.; Rosler, J. Thermodynamic calculations in the development of high-temperature Co-Re-based alloys. *J. Alloys Compd.* **2014**, *582*, 50–58. [[CrossRef](#)]
4. Yamabe-Mitarai, Y.; Ro, Y.; Maruko, T.; Harada, H. Ir-base refractory superalloys for ultra-high temperatures. *Metall. Mater. Trans. A* **1998**, *29A*, 537–749. [[CrossRef](#)]
5. Yamabe-Mitarai, Y.; Harada, H. Design of quaternary Ir-Nb-Ni-Al refractory superalloys. *Metall. Mater. Trans. A* **2000**, *31*, 173–178.
6. Yeh, J.-W.; Chen, S.-K.; Lin, S.-J.; Gan, J.-Y.; Chin, T.-S.; Shun, T.-T.; Tsau, C.-H.; Chang, S.-Y. Nanostructured high-entropy alloys with multiple principal elements: Novel alloy design concepts and outcomes. *Adv. Eng. Mater.* **2004**, *6*, 299–303. [[CrossRef](#)]
7. Tsai, M.-H.; Yeh, J.-W. High-Entropy Alloys: A Critical Review. *Mater. Res. Lett.* **2014**, *2*, 107–123. [[CrossRef](#)]
8. Murty, B.S.; Yeh, J.-W.; Ranganathan, S. *High Entropy Alloys*; Butterworth-Heinemann: London, UK, 2014.
9. Miracle, D.B.; Miller, J.D.; Senkov, O.N.; Woodward, C.; Uchic, M.D.; Tiley, J. Exploration and development of high entropy alloys for structural applications. *Entropy* **2014**, *16*, 494–525. [[CrossRef](#)]

10. Yeh, J.-W. Alloy Design Strategies and Future Trends in High-Entropy Alloys. *JOM* **2013**, *65*, 1759–1771. [[CrossRef](#)]
11. Senkov, O.N.; Senkova, S.V.; Miracle, D.B.; Woodward, C. Mechanical properties of low-density, refractory multi-principal element alloys of the Cr-Nb-Ti-V-Zr system. *Mat. Sci. Eng. A* **2013**, *565*, 51–62. [[CrossRef](#)]
12. Wang, Y.P.; Li, B.S.; Fu, H.Z. Solid solution or intermetallics in a high-entropy alloy. *Adv. Eng. Mater.* **2009**, *11*, 641–644. [[CrossRef](#)]
13. Singh, S.; Wanderka, N.; Murty, B.S.; Glatzel, U.; Banhart, J. Decomposition in multi-component AlCoCrCuFeNi high-entropy alloy. *Acta Mater.* **2011**, *59*, 182–190. [[CrossRef](#)]
14. Senkov, O.N.; Wilks, G.B.; Scott, J.M.; Miracle, D.B. Mechanical properties of Nb<sub>25</sub>Mo<sub>25</sub>Ta<sub>25</sub>W<sub>25</sub> and V<sub>20</sub>Nb<sub>20</sub>Mo<sub>20</sub>Ta<sub>20</sub>W<sub>20</sub> refractory high entropy alloys. *Intermetallics* **2011**, *19*, 698–706. [[CrossRef](#)]
15. Senkov, O.N.; Scott, J.M.; Senkova, S.V.; Miracle, D.B.; Woodward, C.F. Microstructure and room temperature properties of a high-entropy TaNbHfZrTi alloy. *J. Alloys Compd.* **2011**, *509*, 6043–6048. [[CrossRef](#)]
16. Senkov, O.N.; Woodward, C.F. Microstructure and properties of a refractory NbCrMo<sub>0.5</sub>Ta<sub>0.5</sub>TiZr alloy. *Mater. Sci. Eng. A* **2011**, *529*, 311–320. [[CrossRef](#)]
17. Senkov, O.N.; Scott, J.M.; Senkova, S.V.; Meisenkothen, F.; Miracle, D.B.; Woodward, C.F. Microstructure and elevated temperature properties of a refractory TaNbHfZrTi alloy. *J. Mater. Sci.* **2012**, *47*, 4062–4074. [[CrossRef](#)]
18. Senkov, O.N.; Senkova, S.V.; Dimiduk, D.M.; Woodward, C.; Miracle, D.B. Oxidation behavior of a refractory NbCrMo<sub>0.5</sub>Ta<sub>0.5</sub>TiZr alloy. *J. Mater. Sci.* **2012**, *47*, 6522–6534. [[CrossRef](#)]
19. Senkov, O.N.; Woodward, C.; Miracle, D.B. Microstructure and properties of aluminum-containing refractory high-entropy alloys. *JOM* **2014**, *66*, 2030–2042. [[CrossRef](#)]
20. Senkov, O.N.; Senkova, S.V.; Woodward, C. Effect of aluminum on the microstructure and properties of two refractory high entropy alloys. *Acta Mater.* **2014**, *68*, 214–228. [[CrossRef](#)]
21. Senkov, O.N.; Senkova, S.V.; Woodward, C.; Miracle, D.B. Low-density, refractory multi-principal element alloys of the Cr–Nb–Ti–V–Zr system: microstructure and phase analysis. *Acta Mater.* **2013**, *61*, 1545–1557. [[CrossRef](#)]
22. Stepanov, N.D.; Shaysultanov, D.G.; Salishchev, G.A.; Tikhonovsky, M.A. Structure and mechanical properties of a light-weight AlNbTiV high entropy alloy. *Mater. Lett.* **2015**, *142*, 153–155. [[CrossRef](#)]
23. Stepanov, N.D.; Yurchenko, N.Y.; Sokolovsky, V.S.; Tikhonovsky, M.A.; Salishchev, G.A. An AlNbTiVZr<sub>0.5</sub> high-entropy alloy combining high specific strength and good ductility. *Mater. Lett.* **2015**, *161*, 136–139. [[CrossRef](#)]
24. Miller, M.K.; Forbes, R.G. *Atom-Probe Tomography: The Local Electrode Atom Probe*; Springer: New York, NY, USA, 2014.
25. Seidman, D.N. Three-dimensional atom probe tomography: advances and applications. *Annu. Rev. Mater. Res.* **2007**, *37*, 127–158. [[CrossRef](#)]
26. Seidman, D.N.; Stiller, K. An Atom-Probe Tomography Primer. *Mater. Res. Soc. Bulletin* **2009**, *34*, 717–721. [[CrossRef](#)]
27. Miller, M.K.; Russell, K.F.; Thompson, G. Strategies for fabricating atom probe specimens with a dual beam FIB. *Ultramicroscopy* **2005**, *102*, 287–298. [[CrossRef](#)] [[PubMed](#)]
28. Thompson, K.; Lawrence, D.J.; Larson, D.J.; Olson, J.D.; Kelly, T.F.; Gorman, B. *In-situ* site-specific specimen preparation for atom probe tomography. *Ultramicroscopy* **2007**, *107*, 131–139. [[CrossRef](#)] [[PubMed](#)]
29. Sosa, J.M.; Jensen, J.K.; Huber, D.E.; Viswanathan, G.B.; Gibson, M.A.; Fraser, H.L. Three-dimensional characterisation of the microstructure of an high entropy alloy using STEM/HAADF tomography. *Mater. Sci. Technol.* **2015**, *31*, 1250–1258. [[CrossRef](#)]
30. Okamoto, H. *Phase Diagrams for Binary Alloys*, 2nd ed.; ASM International: Materials Park, OH, USA, 2010.
31. Donachie, M.J.; Donachie, S.J. *Superalloys: A Technical Guide*, 2nd ed.; ASM International: Materials Park, OH, USA, 2002.
32. Cahn, J.W. On spinodal decomposition in cubic crystals. *Acta Metall.* **1962**, *10*, 179–183. [[CrossRef](#)]
33. Cahn, J.W. Coherent fluctuations and nucleation in isotropic solids. *Acta Metall.* **1962**, *10*, 907–913. [[CrossRef](#)]
34. Cahn, R.W.; Haasen, P. *Physical Metallurgy*, 4th ed.; North Holland: Amsterdam, The Netherlands, 1996; Volume 1.
35. Binder, K.; Fratzl, P. Spinodal Decomposition. In *Phase Transformations in Materials*; Kostorz, G., Ed.; Wiley-VCH: Weinheim, Germany, 2001; pp. 409–480.

36. Soffa, W.A.; Laughlin, D.E. *Recent Experimental Studies of Continuous Transformations in Alloys: An Overview*; Aaronson, H.I., Laughlin, D.E., Sekerka, R.F., Wayman, C.M., Eds.; AIME: Warrendale, PA, USA, 1982; pp. 159–183.
37. Nishimori, H.; Onuki, A. Pattern formation in phase-separating alloys with cubic symmetry. *Phys. Rev. B* **1990**, *42*, 980. [[CrossRef](#)]
38. Special Metals: Inconel<sup>®</sup> Alloy 718. Available online: [www.specialmetals.com/documents/Inconel%20alloy%20718.pdf](http://www.specialmetals.com/documents/Inconel%20alloy%20718.pdf) (accessed on 1 February 2016).
39. Kaufman, M. Properties of cast Mar-M247 for turbine blisk applications. *Superalloys* **1984**, *1984*, 43–52.
40. Haynes International, High-temperature Tech Brief: HAYNES<sup>®</sup> 230<sup>®</sup> Alloy. Available online: [www.haynesintl.com/pdf/h3060.pdf](http://www.haynesintl.com/pdf/h3060.pdf) (accessed on 1 February 2016).



© 2016 by the authors; licensee MDPI, Basel, Switzerland. This article is an open access article distributed under the terms and conditions of the Creative Commons by Attribution (CC-BY) license (<http://creativecommons.org/licenses/by/4.0/>).